The Effect of Composition Variations on the Response of Steels Subjected to High Fluence Neutron Irradiation

Benjamin M. Jenkins[a]*, James O. Douglas[a], Nathan Almirall[b], Nick Riddle[c], Paul .A.J. Bagot[a], Jonathan M. Hyde[a,d], G. Robert Odette[b], Michael .P. Moody[a]

[a] - Dept. of Materials, Parks Road, Oxford, OX1 3PH, UK
[b] – University of California, Santa Barbara, CA 93106-5050, USA
[c] – Rolls Royce, PO Box 2000, Raynesway, Derby DE21 7XX, UK
[d] – National Nuclear Laboratory, Building D5, First Floor, Culham Science Centre, Abingdon, Oxfordshire, OX14 3DB
* Corresponding author: benjamin.jenkins@materials.ox.ac.uk (B. M. Jenkins)

Keywords
Reactor pressure vessel, neutron irradiation, embrittlement, atom probe tomography, solute clustering

Abstract
A set of low alloy model reactor pressure steels, with systematic variations in their Mn, Ni, and Si contents, were neutron-irradiated to high fluence (1.4 x 10^{20} n/cm^2) in the Advanced Test Reactor at Idaho at 290 °C and a flux of 3.6 x 10^{12} n/cm^{2}s. The alloys were analysed using atom probe tomography and solute clusters were observed in each alloy, including in one alloy that contained low nominal levels of Mn (0.04 at. %) and Si (0.06 at. %). Changes in the mechanical properties of the alloys were correlated with cluster volume fractions. Whilst the effect of nominal composition was observed to influence cluster composition, cluster nucleation site was not observed to affect composition. Several grain boundaries were also analysed and the segregation of behaviour of certain elements is discussed.

1. Introduction
The reactor pressure vessel (RPV) is the primary containment vessel in light water nuclear reactors and safe operation is achieved through demonstration of an exceptionally low likelihood of failure throughout the operational lifetime. The degradation in the mechanical properties of the RPV limits the safe operational lifetime of the component and, since the RPV is prohibitively expensive to replace, the service life of the power plant. Due to the high initial costs associated with nuclear power plant construction it is essential to maximise their safe operating lifetimes.

Extending the lifetime of reactors, whilst still ensuring the risk of component failure remains acceptably low, requires the development of models that can accurately predict the evolution of the mechanical properties of the RPV during service. However, such models first require a comprehensive understanding of the mechanisms responsible for embrittlement processes. Furthermore, any predictive models must also be validated by comparison with experimental data[1].

Previous work demonstrated that the residual Cu content in early RPVs resulted in the formation of Cu-rich precipitates, these precipitates inhibited dislocation motion and led to embrittlement during service[2–7]. As a result, the target Cu content of RPV steels was reduced. However, these low-Cu steels were still found to embrittle when exposed to high levels of neutron irradiation, due to the formation of Mn-Ni-Si-rich clusters/precipitates[8–15].

As an increasing number of power plants apply for lifetime extensions of up to 80 years, there is increased interest in observing and understanding the response of RPV steels that have been exposed to high neutron fluences. In particular, there is a need to understand the embrittlement of low-Cu steels and to investigate the formation of Mn-Ni-Si-rich features and

other features that may lead to hardening. Furthermore, the grain boundary embrittlement phenomena, due to the segregation of P and other solutes[16,17], must also be understood and accounted for at extended lifetimes.

In this article, the response of four low-Cu steels irradiated to a neutron fluence of 1.4 x 10^{20} n/cm^2 is reported. There were systematic variations in the Mn, Ni, and Si contents of the steels. The nature of Mn-Ni-Si solute clustering/precipitation observed in the matrix of each alloy is discussed with respect to alloy composition. The segregation behaviour of elements to grain boundaries in a selection of the alloys is also discussed, as are some of the advantages and limitations in using APT to characterise these features.

2. Materials and Methods

2.1. Materials

Four steels were neutron irradiated in the Advanced Test Reactor (ATR-2) experiment. The alloys were neutron-irradiated to a fluence of 1.4 x 10^{20} n/cm^2 at a flux of 3.6 x 10^{12} n/cm^{2}s and an irradiation temperature of 290 °C (equivalent to 0.17 displacements per atom).

The nominal composition of each steel is shown in Table 1. Prior to irradiation, three of the steels (C, G, and K) were forged and then rolled to 25 mm in thickness. These steels then underwent austenitization at 920 °C for one hour before they were air cooled and tempered at 600 °C for five hours. Finally, the steels were air cooled to room temperature, resulting in a bainitic-martensitic microstructure. Alloy RX12 was a forged material in the quenched and tempered condition. RX12 contained higher Cr content than the other alloys. However, as Cr has not previously been reported to influence the formation of Mn-Ni-Si-rich features, in the initial design of this experiment it was assumed that its effect on the extent of the formation of these clusters is negligible.

Alloy	Cu	Si	Ni	Mn	P	Cr	Mo	C	Fe
C (A32)	0.04	0.37	3.11	1.90	0.01	0.10	0.27	0.87	Bal.
G (A31)	0.04	0.38	1.54	1.93	0.01	0.10	0.28	0.88	Bal.
K (A26)	0.04	0.38	3.16	0.24	0.01	0.10	0.28	1.10	Bal.
RX12 (AX12)	0.02	0.06	3.22	0.04	0.00	1.84	0.31	0.96	Bal.

Table 1: Nominal composition (at. %) of the alloys used in the study. The alloy names in parentheses indicate the name assigned to the alloys by collaborators at UCSB.

2.2. Methods

2.2.1. Microhardness Testing

Vickers microhardness tests were performed on a modified LECO 400 series instrument, using a diamond pyramid indenter at a 0.5 kg load with a 10 second dwell time. Each 3 mm diameter disc had a thickness of 0.5 mm and was loaded in a multi-disc holder, and polished on a Buehler Vibromet with colloidal silica suspension down to 0.05 µm. The Vickers indenter was used to create a minimum of ten indents per specimen. The Vickers hardness (Hv) was calculated by measuring the diagonal lengths of the indents with a 40x digital microscope. To avoid sampling volumes of the material that had been plastically deformed by previous indents, the spacing between indents was greater than 3 times their size[18]. If the difference between two indent diagonal lengths was greater than 5%, the data was discarded. The average and standard deviation from unirradiated and irradiated specimens was tabulated.

2.2.2. Focused Ion Beam Sample Preparation

After irradiation, 3 mm disc specimens were mechanically ground and polished to a 1 µm surface finish. These specimens were prepared for atom probe tomography (APT) analyses using a FEI Quanta 3D FEG focused ion beam. Standard lift-out and preparation procedures were followed[19,20]. A final polish of 5 kV was applied to each sample to minimise Ga damage in the analysis volume.

2.2.3. Atom Probe Analyses

Atom probe analyses were conducted on a LEAP-4000X HR at Idaho National Laboratory. All analyses were conducted in voltage mode at an operating temperature of 50 or 55 K and a pulse fraction of 20 %. Pulse frequencies of 200 kHz and a target detection rate of 0.003 ions per pulse were applied.

Reconstructions of the APT data were created using IVAS 3.8.0. Each reconstruction was calibrated by matching the interplanar spacing at crystallographic poles in the data to the interplanar spacing of the corresponding directions in BCC α-Fe. If poles were not present in the data, parameters were selected such that the atomic density of the reconstructed volume, after accounting for the imperfect detection efficiency of the instrument, was consistent with that of α-Fe.

Cluster searches were conducted implementing the core-linkage algorithm tool in IVAS 3.8.0[21], which is a variant of the maximum separation method[22]. Cluster search parameters were chosen to maximise detectability (whilst avoiding cluster linking/splitting[23]) by sweeping through D_{max}, NN_{order}, and N_{min}, and then comparing the results to those obtained from a dataset in which the chemical identities of the ions were randomly shuffled[24]. Nearest neighbour order values of between 1 - 10 were utilised. Meanwhile, D_{max} = 0.45 - 0.65 nm; the envelope (L) and erosion (E) parameters were set to half the D_{max} value used in each analysis, whilst N_{min} values ranged between 10-40. Ions included in the cluster search included Cu, Ni, Mn, Si, and P; the Fe-Ni peak overlap at 29 Da was included in the cluster analysis but was deconvoluted when calculating cluster compositions.

Cluster volume fractions, sizes, and number densities, ~~and compositions~~ were calculated using the equations detailed in the Appendix. Previous research has indicated that trajectory aberrations in the atom probe experiment, which arise due to the difference in evaporation field between the matrix and the features[25], result in APT measurements overestimating the Fe content of clusters rich in Cu[26], Si, and Mn[15]. Therefore, in this study Fe has been removed from size, volume fraction, or composition calculations (unless otherwise stated). Individual cluster compositions were calculated by assuming that all ions that had a mass-to-charge-state ratio of 29 and were detected in the cluster were Ni. This is a good approximation due to the high Ni content in the clusters and because, given the small sizes of the clusters, the contribution of $^{58}Fe^{2+}$ to the 29 Da peak is very small (the isotopic abundance of $^{58}Fe^{2+}$ is 0.28 at. %). Cluster sizes were estimated by assuming the clusters were spherical and using the number of atoms detected in each cluster after correcting for the imperfect detection efficiency of the instrument. Clusters that intersected the edge of the analysed volume were identified using the methods outlined in [27]; these clusters were counted as half a cluster for number density calculations and were not included in size or composition calculations. Clusters nucleated on carbide-matrix interfaces, or within carbides were not included in compositional calculations or volume fraction.

Grain boundary analyses were performed at multiple locations across each grain boundary. At each location, a region of interest (ROI) was placed perpendicular to the grain boundary such that a 20 x 20 nm area of the grain boundary was contained within the ROI. A one-dimensional concentration profile was created along each ROI and the composition of the

grain boundary was calculated as described in [28]. Changes in grain boundary composition as a result of density fluctuations with respect to the matrix were accounted for using the method outlined by Blavette et al. [29]. Whilst this will improve the accuracy of grain boundary composition measurements, the quantitative accuracy of grain boundary compositional measurements made via APT are subject to artefacts[30] that this simple correction does not fully account for.

3. Results

3.1. Microhardness Change During Irradiation

Each of the alloys displayed an increase in hardness from their non-irradiated condition (Figure 1). Alloy C contained high levels of Ni and Mn and exhibited the largest increase in hardness after irradiation. Meanwhile Alloy RX12, which contained very low levels of Mn and Si, had the smallest hardness increase of the four alloys after irradiation.

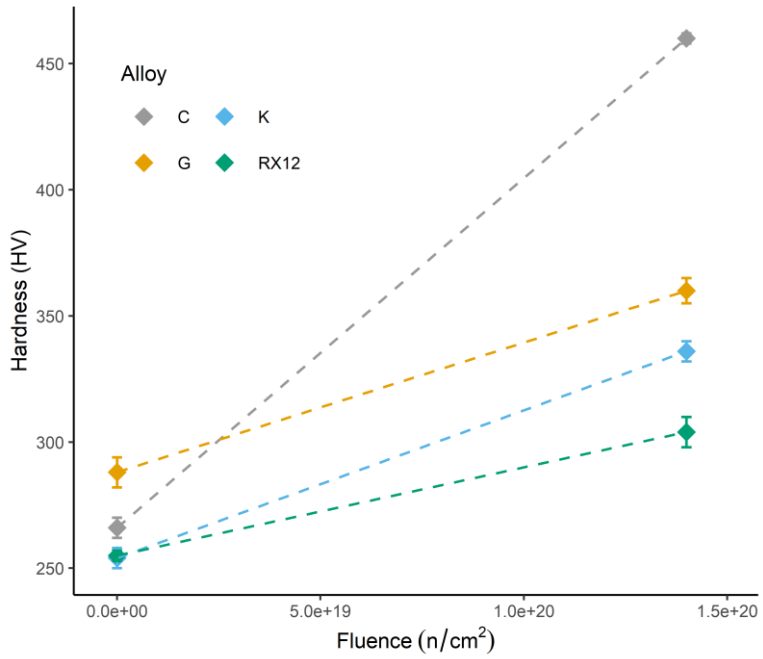

Figure 1: Evolution in hardness (HV) of the alloys after exposure to neutron irradiation (Fluence = 1.4 x 10^{20} n/cm^2, flux = 3.6 x 10^{12} n/cm^{2}s, T_{iir} = 290 °C). Error bars represent the standard deviation of the mean.

3.2. Atom Probe Tomography Results

A non-random distribution of solute (Cu, Ni, Mn, Si, P) atoms was observed in each dataset for each alloy. This could be seen upon visual inspection and quantitative data were acquired by performing cluster searches.

3.2.1. Measured Alloy Composition

Carbides were observed in several reconstructions for Alloy C and one reconstruction for Alloy G. Since carbides were not observed in the APT analyses for each of the respective alloys, the composition of the tips analysed in this study were calculated after carbides had been removed from the datasets. Peak overlaps were solved using Atom Probe Lab v0.1.3[31] which implements the methods outlined by London[32]. The mean of these compositions are shown in Table 2.

Alloy	Cu	Si	Ni	Mn	P	Cr	Mo	C	Fe

C	0.04 ± 0.00	0.45 ± 0.01	3.17 ± 0.07	1.24 ± 0.05	0.01 ± 0.00	0.07 ± 0.01	0.13 ± 0.01	0.23 ± 0.07	94.67 ± 0.16
G	0.03 ± 0.00	0.35 ± 0.02	1.44 ± 0.02	1.15 ± 0.04	0.00 ± 0.00	0.06 ± 0.00	0.20 ± 0.01	0.29 ± 0.25	96.47 ± 0.18
K	0.04 ± 0.00	0.38 ± 0.01	3.39 ± 0.05	0.21 ± 0.01	0.00 ± 0.00	0.11 ± 0.01	0.23 ± 0.01	0.09 ± 0.02	95.53 ± 0.06
RX12	0.02 ± 0.00	0.07 ± 0.03	3.54 ± 0.18	0.05 ± 0.01	0.00 ± 0.00	1.09 ± 0.03	0.17 ± 0.02	0.03 ± 0.01	95.02 ± 0.17

Table 2: Mean observed composition (at.%) of the APT tips analysed in this study. Error is indicative of the standard error of the mean of different tip compositions. N.B. Carbide regions were not included in these calculations.

The compositions measured using APT are very similar to the nominal compositions (Table 1). The only elements that were measured in significantly lower amounts when using APT were Mn, Mo, and C. This is to be expected as these elements are carbide formers and are present in high concentrations within carbides.

3.2.2. Alloy C (0.37 Si, 3.11 Ni, 1.90 Mn (at.%))

Seven APT datasets (N = 7) were successfully obtained for Alloy C; an atom map for one of these datasets is shown in Figure 2. A non-random distribution of Mn, Ni, Si, and P is evident and the segregation behaviour of Ni and P atoms to a planar feature indicates the presence of a grain boundary in this dataset. A carbide, enriched in Mn, was also observed to have formed on the grain boundary. Grain boundaries were detected in five datasets for Alloy C and various degrees of solute segregation was detected at each of these features. Discrete solute clusters were observed to have formed at numerous locations along the grain boundaries.

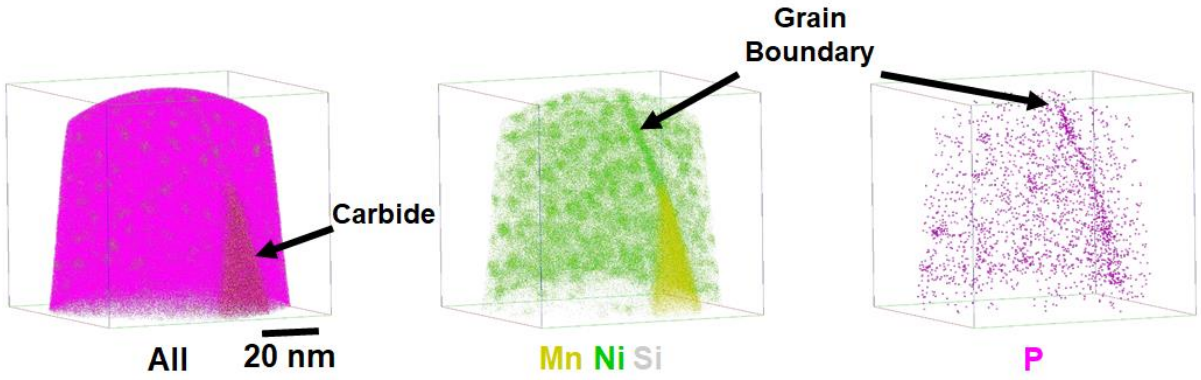

Figure 2: Atom maps for a dataset from Alloy C. The grain boundary and carbide regions are indicated.

3.2.3. Alloy G (0.38 Si, 1.54 Ni, 1.93 Mn (at.%))

Clustering was also detected in all of the datasets (N = 3) from Alloy G (Figure 3). The clusters were enriched in Mn, Ni, Si, and P. Several of the features were observed to have formed on linear features that were enriched in P. These are likely to be heterogeneous nucleation sites, such as dislocations. The composition of the clusters that formed on heterogeneous nucleation sites was not found to be significantly different from the composition of those that were observed to have nucleated homogeneously. This is discussed in more detail in Section 4.4.

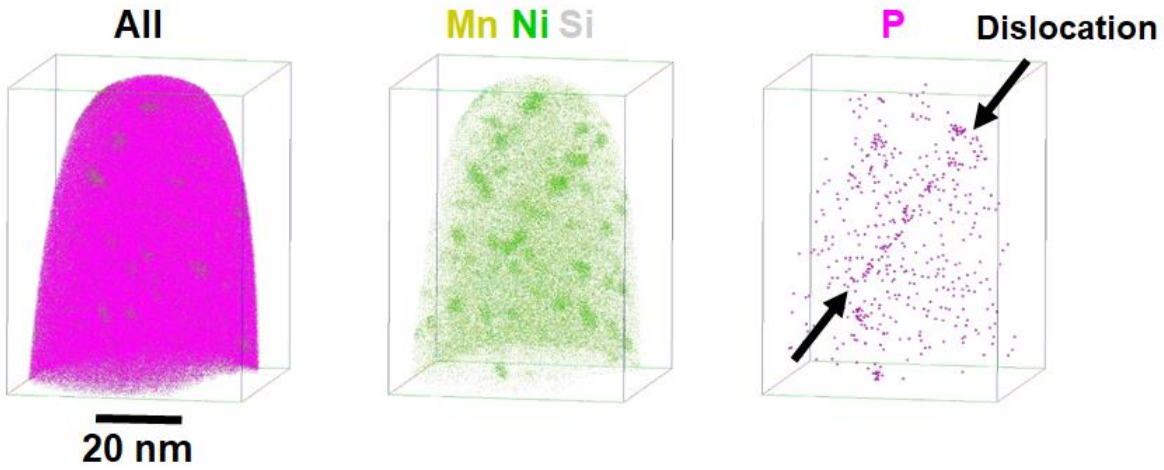

Figure 3: Atom maps for a dataset from Alloy G showing the distribution of Mn, Ni, and Si, and P.

3.2.4. Alloy K (0.38 Si, 3.16 Ni, 0.24 Mn (at.%))

Figure 4 shows the atom maps for a dataset that is representative of the twelve datasets collected for Alloy K. Clustering was detected in all of the datasets. Similar to Alloy G, some clusters appeared to have formed on heterogeneous nucleation sites.

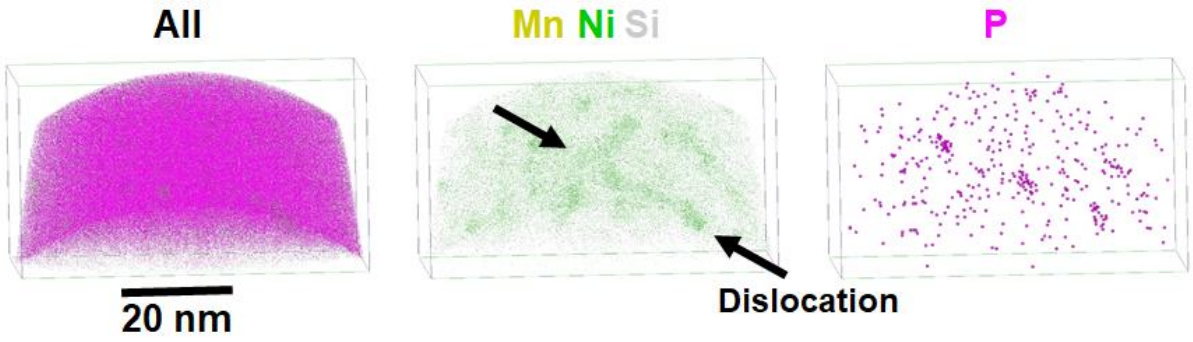

Figure 4: Atom maps for a dataset from Alloy K showing the distribution of Mn, Ni, and Si, and P. A linear feature, enriched in Mn, Ni, and Si is highlighted by the arrows.

3.2.5. Alloy RX12 (0.06 Si, 3.22 Ni, 0.04 Mn (at.%))

Two datasets were successfully obtained for alloy RX12. Figure 5 shows a dataset that contained a higher density of linear features than the other alloys; these features were enriched in Ni and are likely to be dislocations. The enriched P region was located at the intersection point between two of these dislocations.

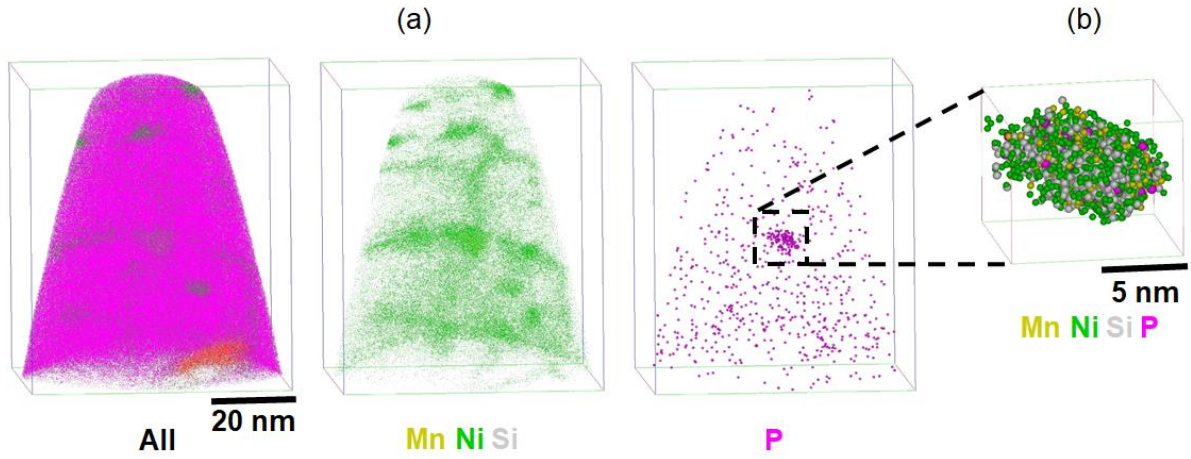

Figure 5: (a) Atom maps for RX12 showing the distribution of Mn, Ni, Si, and P. (b) Enlarged map showing distribution of Mn, Ni, Si, and P atoms in the region highlighted in (a).

3.3. Cluster Analyses

Table 3 displays the mean cluster statistics that were calculated after the cluster search algorithms had been applied to every dataset collected for each respective alloy. The cluster statistics for Alloy RX12 are shown for both when Fe is included and excluded from the calculations; the reasoning for this is that evidence suggests that Fe detected in the clusters in this alloy is more likely not the result of evaporation artefacts, in comparison to the clusters observed in the other alloys, and this is discussed in more detail later.

Alloy C exhibited the highest number density and volume fraction of clusters followed by Alloy K. Alloys G and RX12 had the lowest mean number density and volume fraction of clusters of the four alloys. However, due to tip-to-tip variability resulting in variance in the measurements, there was no significant difference between the number density of clusters detected in Alloy G and RX12. Although, the average diameter of the clusters detected in RX12 was smaller than the average of clusters identified in Alloy G.

Alloy	Estimated Volume Sampled (x 10^{-23} m^3)	Note	Number Density (x10^{23} /m^3)	Diameter (nm)	Volume Fraction (%)
C	10.4		21.2 ± 1.0	2.44 ± 0.19	2.09 ± 0.11
G	1.67		7.5 ± 0.4	2.13 ± 0.09	0.55 ± 0.10
K	6.97		11.5 ± 1.5	1.92 ± 0.03	0.78 ± 0.04
RX12	1.49	Exc. Fe	7.0 ± 4.2	1.50 ± 0.12	0.65 ± 0.23
		Inc. Fe		1.78 ± 0.14	1.08 ± 0.32

Table 3: Observed cluster details for the four alloys, along with the estimated volume sampled from each material. The N_d and V_f errors are representative of the standard error of the mean calculated from the variance between datasets for each alloy. Meanwhile, the error in cluster diameter is calculated from the entire cluster population for each alloy. N.B. Cluster characteristics are provided for RX12 both including and excluding Fe.

The ratio of Mn:Ni:Si in the clusters was plotted on a Gibbs triangle (Figure 6 (a)). For each alloy, the set of identified clusters was divided up into quartiles based on cluster size, with the Mn:Ni:Si ratio calculated for each size quartile for each alloy. It was observed that the mean cluster composition of the largest quartile of clusters was significantly different to the smallest quartile of clusters.

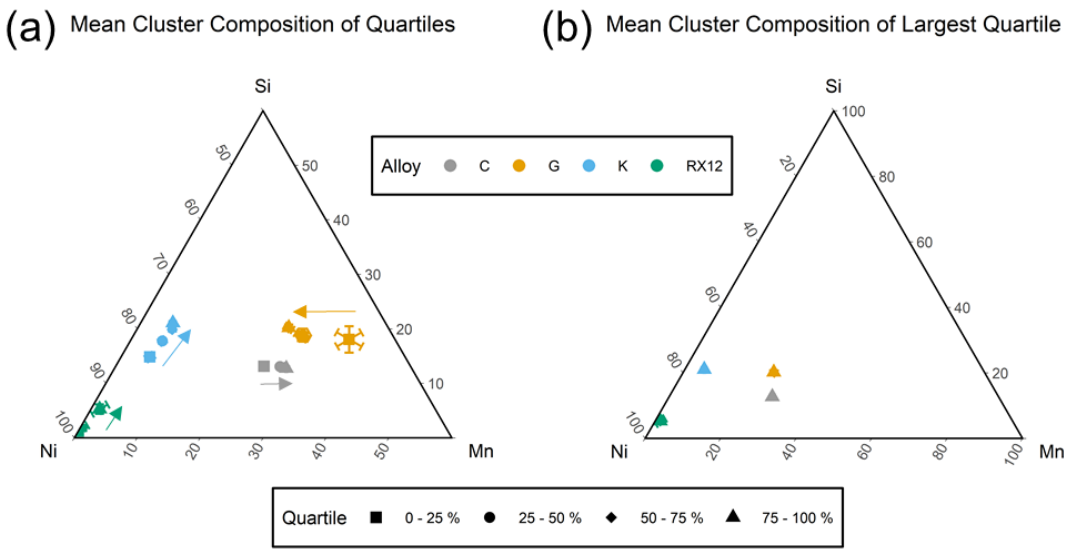

Figure 6: (a) Gibbs' triangle section showing Mn:Ni:Si ratios for each quartile (size) of clusters for each alloy. Arrows indicate the development of Mn:Ni:Si ratio as cluster sizes increase. (b) Gibbs triangle displaying Mn:Ni:Si ratio for the largest 25 % of clusters detected in each alloy. Error bars represent the standard error of the mean for each quartile of clusters sampled within each alloy.

The average composition of the largest 25 % of clusters detected in each alloy is shown in Table 4. Ni, Mn and Si accounted for a large fraction of the solute detected in the clusters in all of the alloys.

Alloy	N	Note	Ni	Mn	Si	Cu	P	Other	Fe
C	373/1493		58.5 ± 0.1	26.6 ± 0.2	12.4 ± 0.1	1.4 ± 0.0	0.2 ± 0.0	0.9 ± 0.0	46.2 ± 0.2
G	23/92		54.0 ± 0.5	23.2 ± 0.8	19.5 ± 0.6	1.6 ± 0.1	0.8 ± 0.2	0.9 ± 0.1	46.3 ± 0.6
K	151/606		71.4 ± 0.3	5.0 ± 0.2	20.4 ± 0.2	1.7 ± 0.1	0.3 ± 0.0	1.3 ± 0.1	43.4 ± 0.4
RX12	17/70	Exc. Fe	90.9 ± 1.6	1.3 ± 0.6	5.2 ± 0.8	0.7 ± 0.1	0.2 ± 0.1	1.7 ± 0.3	
		Inc. Fe	52.7 ± 0.9	0.8 ± 0.3	3.0 ± 0.5	0.4 ± 0.1	0.1 ± 0.1	1.0 ± 0.2	42.0 ± 0.8

Table 4: Mean compositions (at. %) of the largest 25 % of non-edge clusters detected in each alloy (excluding Fe). The standard error of the mean for each measurement is also provided. N.B. Whilst the authors believe that the majority of the Fe detected in the clusters in Alloys C, G, and K is due to aberrations, it is included for reference for those who interpret the data differently.

3.4. Grain Boundary Analyses

Grain boundaries were detected in datasets from five datasets from Alloy C and one dataset from Alloy K. The composition of the grain boundary regions varied from specimen-to-specimen and between alloys. However, Ni, P, Cu, and Si were observed to segregate to all of the grain boundaries.

Figure 7 show the composition of the grain boundary regions analysed in Alloy C. The composition of the grain boundaries in Alloy C contained more Ni, P, Cu, and Si than the nominal composition of the alloy. All but one of the grain boundaries analysed in Alloy C had a higher Mn composition than the nominal composition.

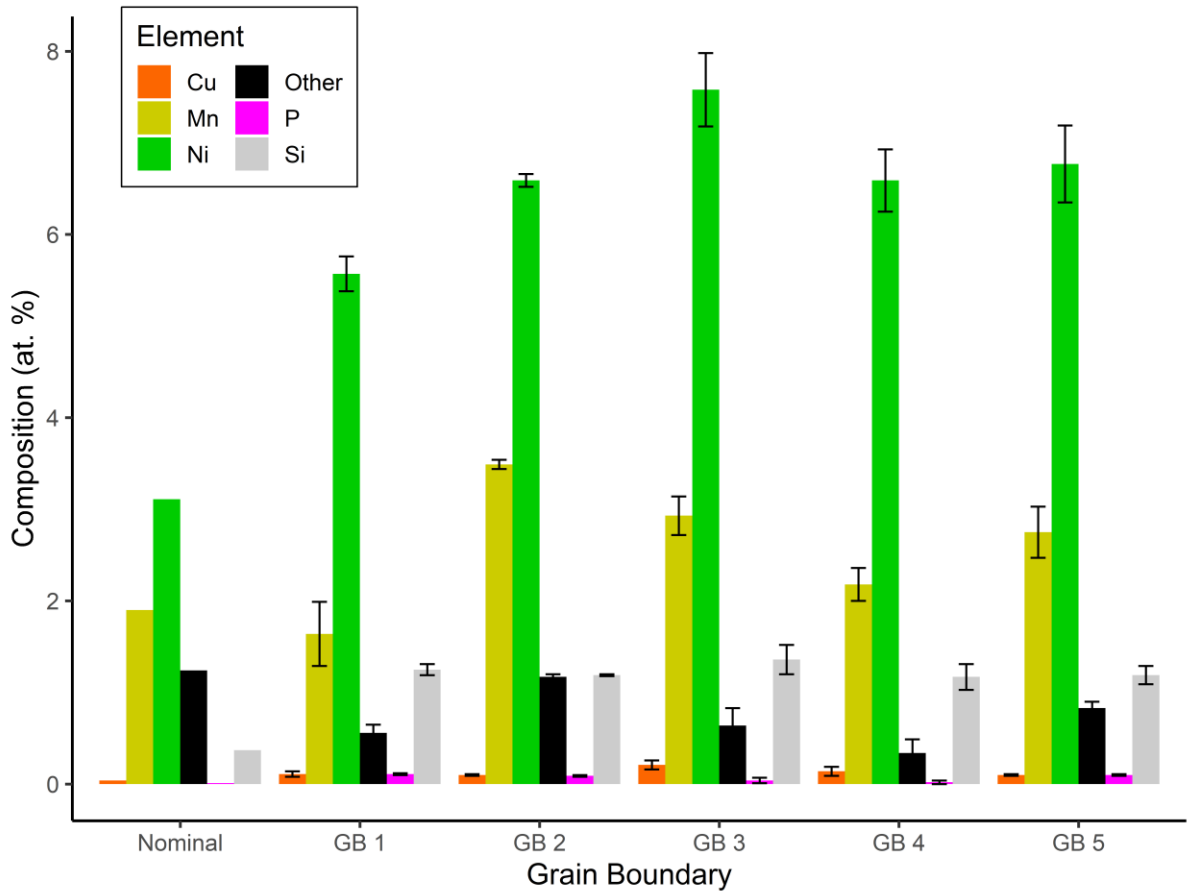

Figure 7: Graph showing the measured composition (at. %) of the grain boundaries in Alloy C compared to the nominal composition (Fe is not shown for clarity).

Table 5 contains the measured composition of the grain boundary sampled in Alloy K. The grain boundary contained more C, Cu, Mn, Ni, P, Si, and Mo than the alloy's nominal composition; Figure 8 shows this graphically.

Element	Composition (at. %)
C	1.89 ± 0.08
Cr	0.09 ± 0.01
Cu	0.11 ± 0.00
Fe	86.08 ± 0.56
Mn	0.46 ± 0.04
Mo	0.91 ± 0.03
Ni	8.82 ± 0.30
P	0.03 ± 0.00
Si	1.60 ± 0.11

Table 5: Composition (at. %) of the grain boundary sampled in Alloy K.

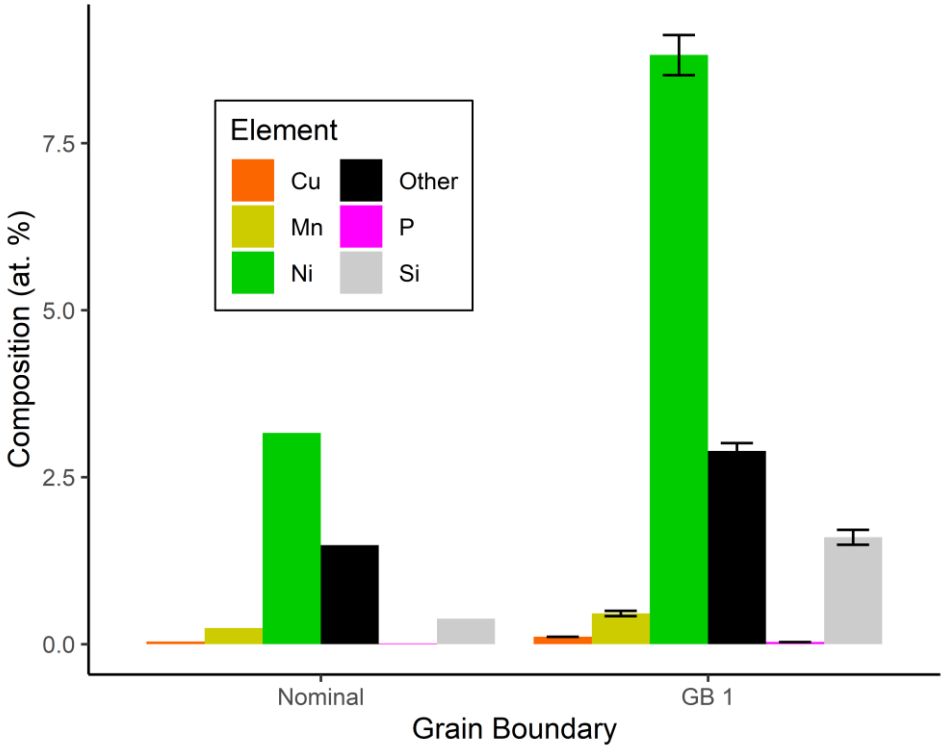

Figure 8: Graph showing the measured composition (at. %) of the grain boundary in Alloy K compared to the nominal composition (Fe is not shown for clarity).

4. Discussion

4.1. Relationship Between Mechanical Property Changes and Clustering

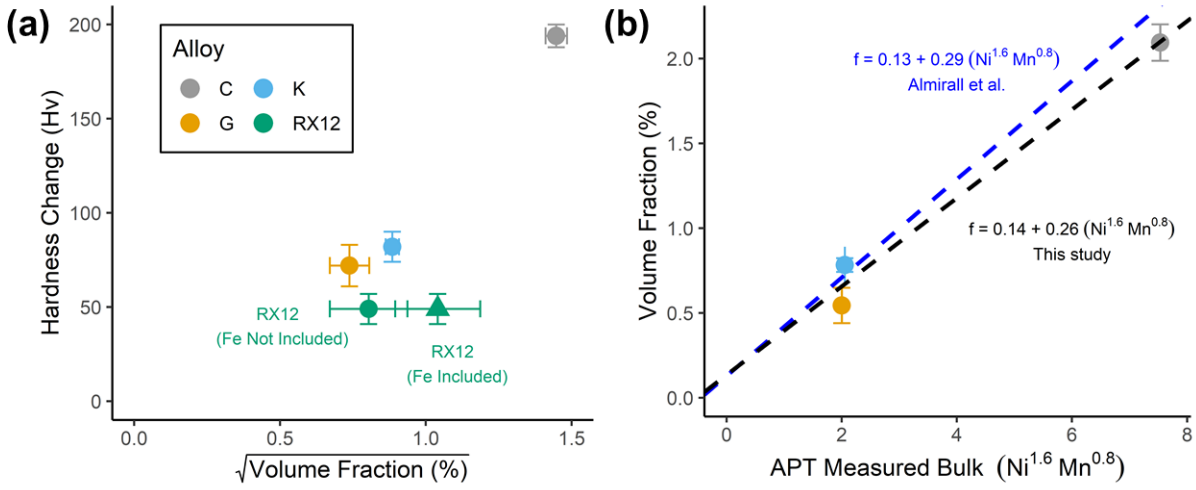

Figure 9: (a) Plot of $\sqrt{Volume\ Fraction}$ of clusters detected in each alloy vs hardness change (HV). (b) Plot of Chemistry factor proposed by Almirall et al. [33] against cluster volume fraction for Alloys C, G, and K.

There was a correlation between larger increases in hardness during irradiation and the formation of larger cluster volume fractions in Alloys C, G, and K (Figure 9 (a)). The Russell-Brown hardening model predicts that hardness will increase proportionally with the square root of Cu-rich precipitate volume fraction[34] for obstacles of the same size and modulus (composition/structure). However, even when Fe was included in the volume fraction calculations for alloy RX12, it did not appear to fit the same trend-line as the other three alloys. The fact that the observed cluster compositions in RX12 differed significantly from

the other three material conditions (significantly richer in Ni coupled with a potentially higher Fe content) may explain why it did not appear to fit the same trend-line as the other three alloys.

Almirall et al. observed that a chemistry factor of $Ni^{1.6}Mn^{0.8}$, where Ni and Mn are the mean measured composition of Ni and Mn in the APT datasets, correlated well with measured cluster volume fraction in a series of alloys that had been irradiated to the same fluence as the specimens used in this study[33]. Figure 9 (b) shows the relationship between the chemistry factor and cluster volume fraction for Alloys C, G, and K. The data for RX12 was considered an outlier and not included in the model. To permit direct comparison with the Almirall et al. paper, Fe was not included in the calculations for volume fractions used in this plot or the linear models fitted to the data. Whilst the coefficients used by Almirall et al. [33] ($V_f = 0.13 + 0.29Ni^{1.6}Mn^{0.8}$) fit the data in this study well, the least squares fit to the data had different coefficients ($V_f = 0.14 + 0.26Ni^{1.6}Mn^{0.8}$), with a slightly larger intercept and lower gradient.

4.2. Fe Content of Clusters in RX12

The majority of Fe detected within Cu-rich precipitates in APT experiments is thought to be the result of trajectory aberrations that arise due to a local magnification effect caused by the lower evaporation field of the Cu-rich precipitates, which are mainly comprised of Cu atoms, in comparison to the Fe-rich surrounding matrix[35]. The evaporation field of pure Cu is 30 Vnm^{-1} [36] whilst pure Fe has a higher evaporation field of 35 Vnm^{-1} [37]. The artefact of these trajectory aberrations can be seen in APT reconstructions whereby the apparent density of the Cu-rich precipitates is measured to be unphysically high and much higher than the surrounding matrix.

Since the evaporation fields of Mn (30 Vnm^{-1}) and Si (33 Vnm^{-1}) are also lower than that of Fe[9], it is expected that Mn-Ni-Si-rich precipitates may have a lower evaporation field than the surrounding matrix and will therefore be subjected to similar trajectory aberrations. Indeed, atomic density maps within the reconstructed APT data revealed that the Mn-Ni-Si-rich clusters in Alloy C had a much higher density than the surrounding matrix (Figure 10 (a)). Correlative work has shown that APT experiments do overestimate the Fe content of Mn-Ni-Si-rich precipitates[15]. However, the exact degree to which APT overestimates the Fe content of these precipitates is still debated and is likely to be a function of precipitate size and composition.

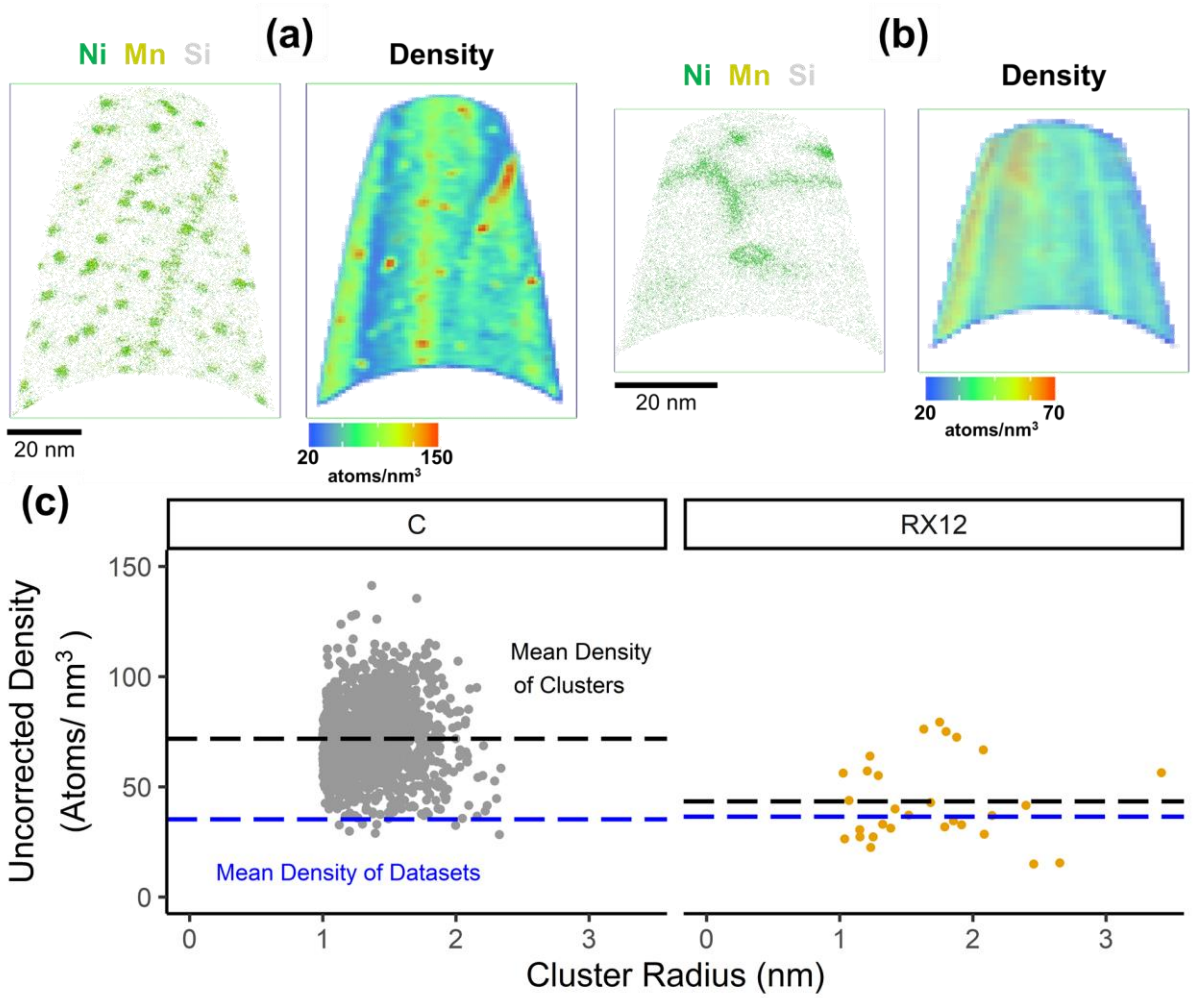

Figure 10: (a) Atom maps of Ni, Mn and Si atoms and density plot of atom map in Alloy C. (b) Atom maps of Ni, Mn and Si atoms and density plot of atom map in Alloy RX12. (c) Graph of density of measured atoms per nm^3 against cluster radius (for radius ≥ 1 nm) – mean cluster density and overall dataset density is also plotted.

As most of the clusters in RX12 contained low levels of Mn, Si, and Cu, it is possible that the impact of trajectory aberrations on these features would be significantly smaller. Density plots of the APT reconstructions from RX12 revealed the clusters had a very similar density to the surrounding matrix (Figure 10 (b)). In comparison, the mean density of atoms per unit volume within the clusters in Alloy C were significantly larger ($p < 0.05$) than the density of the atoms within the clusters observed in RX12. In the case of Ni-rich precipitates, trajectory aberrations are unlikely to be as prevalent because pure Ni and Fe have a similar theoretical evaporation field (35 Vnm^{-1})[37]. Due to the lack of density variations observed in RX12, the majority of the Fe detected in the clusters in these specimens is likely to be real and not an experimental artefact.

Assuming that the Fe detected in the clusters in RX12 is real, the clusters have a mean composition of 54 Ni – 41 Fe – 5 Other (at. %). This composition is near the transition between the FeNi and $FeNi_3$ phase fields at 290 °C[38]. A previous TEM/APT study has observed Fe_3Ni precipitates in an ion-irradiated binary alloy[39]. It is, therefore, ~~reasonable~~ probable that this study is the first to report ~~that~~ the formation of Fe_xNi_y-type features ~~observed in this study have formed~~ under neutron-irradiation in steels that contain low nominal levels of Mn and Si. The observation that these features can form in low Mn and low Si steels must be accounted for in lifetime prediction models of the RPV component.

4.3. Effect of Size on Cluster Composition

Figure 6 demonstrates that there was a larger variance in the measured composition of the smaller clusters in each alloy and that the mean Mn:Ni:Si ratio of the clusters changed for each size quartile.

Due to the heterogeneous nature of the local composition of small volumes throughout the matrix in any material, cluster compositions are expected to display a degree of variance when clusters are in the early stages of formation. This is due to two effects, one statistical and one physical. Firstly, at small cluster sizes, small variations in the number of atoms of a certain species in the cluster have a larger influence on the composition of the cluster than when there are many atoms in the clusters. Therefore, the large degree of variance in the composition of the smaller clusters may be a result of small variations in the number of atoms of each species in the early-stage clusters. Secondly, in the early stages of cluster formation, a cluster's composition is expected to represent the composition of the region immediately surrounding the atoms which cluster together (since diffusion distances are small at low times). As a result, there is likely to be a variation in the number of atoms of a certain species in each cluster when the clusters are small. As the clusters grow, the range of cluster compositions was observed to decrease.

Since cluster composition is likely to be influenced by the composition of the matrix region which immediately surrounds the cluster, early-stage clusters are unlikely to have a composition that is representative of a thermodynamically-stable phase. As the clusters grow in size due to the diffusion of atoms from further away, the composition of the feature should tend towards a stable/metastable composition. This may explain why the mean Mn:Ni:Si ratio and composition of the clusters changes as they increase in size.

As it is expected that the larger clusters are more likely to be close to the thermodynamically stable composition of the clusters, the mean compositions for the largest 25 % of clusters is provided in Table 4.

4.4. Effect of Nucleation Site on Composition

Clusters were observed to have formed on heterogeneous nucleation sites in each of the alloys. Despite it being possible to determine the nucleation site of clusters from atom probe data, it is uncommon to investigate if or how nucleation site influences cluster composition. Nucleation sites included grain boundaries, dislocations, and carbide-matrix interfaces. The mean Mn:Ni:Si ratio of clusters detected on each nucleation site in samples C, G, and K is shown in Figure 11. No significant difference in Mn:Ni:Si ratio was observed for clusters on different nucleation sites, except for clusters that had nucleated within a carbide in Alloy C. Since the composition of carbides are vastly different to the matrix composition, it is unsurprising that this observation was made.

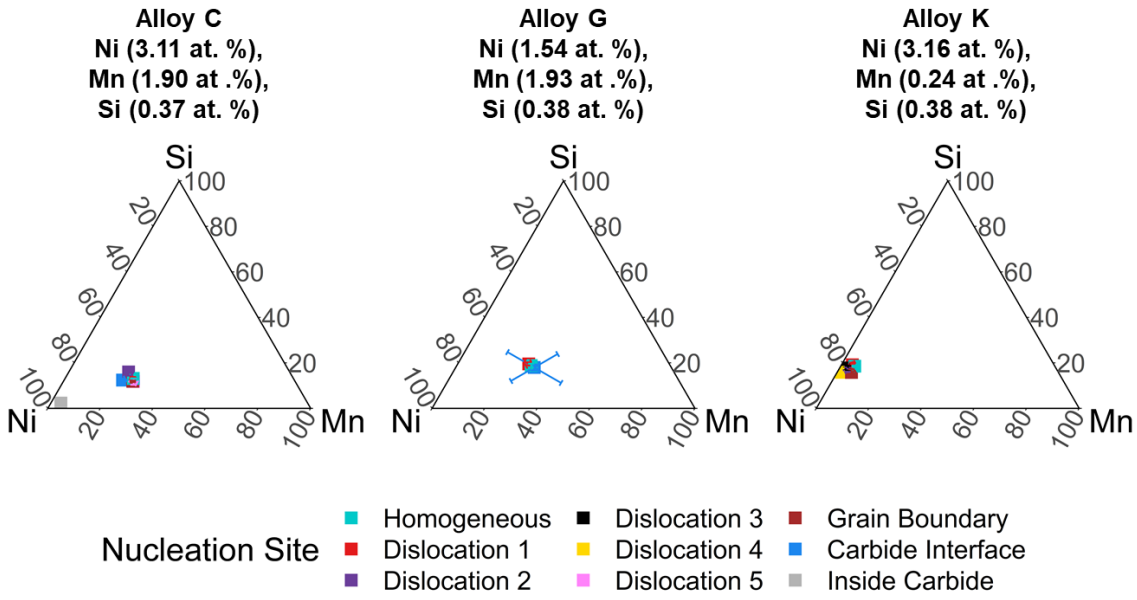

Figure 11: Gibbs triangles showing the mean M:Ni:Si ratio of clusters detected on each type of nucleation site for alloys C, G, and K.

As the majority of the Fe detected within the RX12 clusters is not believed to be the result of aberrations, Gibbs triangles do not accurately represent the composition of the clusters. However, they do provide a suitable visualisation of the Mn:Ni:Si ratio within the clusters. Gibbs triangles showed there was a large fluctuation in the Mn:Ni:Si ratio of a cluster at one nucleation site in the RX12 samples. The cluster, which contained large fractions of Mn and Si, was observed at the intersection point of two dislocations. The cluster also contained a large number of P atoms (Figure 5 (b)).

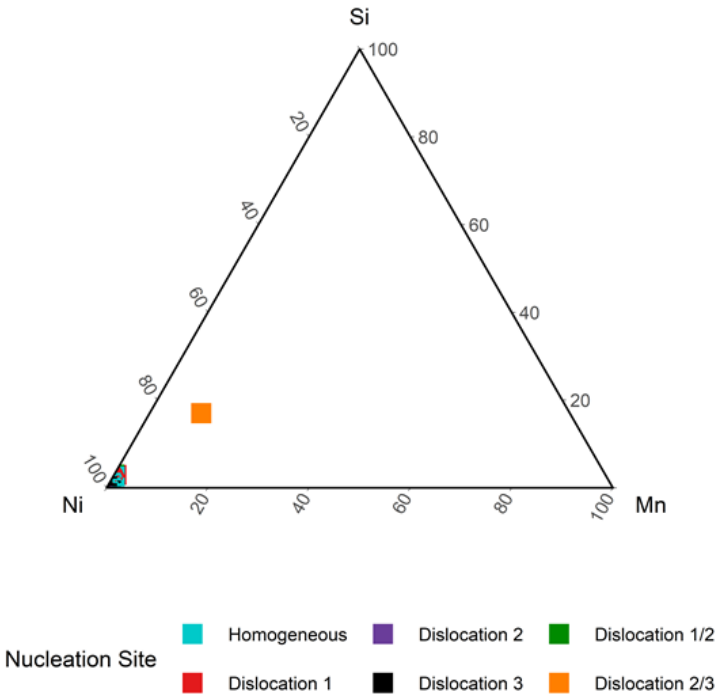

Figure 12: Gibbs triangle showing ratio of Mn:Ni:Si for clusters detected in RX12.

This cluster was the largest detected in this alloy. This may have been a result of the two dislocations acting as fast diffusion pathways, allowing more solute atoms to diffuse to this cluster than to other clusters during irradiation. The Mn, Si, and P content of the cluster may be because this nucleation site was the most energetically favourable for these elements to coalesce around. If this cluster was excluded from mean composition calculations, the clusters in RX12 contained almost no Mn, Si, or P.

Thermodynamic models are often used to predict cluster volume fractions and equilibrium compositions in RPV steels [11,40]. It is, therefore, important that reported cluster compositions do not include those clusters that have formed within carbides, particularly if they are to be used to validate or inform models.

No significant difference in cluster size was observed between the different nucleation sites in alloys C, G, and K. However, a slightly higher number density of features was detected.

4.5. Grain Boundary Segregation

Solute segregation was observed to grain boundaries in six datasets. Not only did the composition of grain boundaries vary between alloys, but some of the grain boundaries in Alloy C had significantly different compositions to one another. This variation in the composition of grain boundaries in Alloy C may be a result of the grain boundaries being located near other microstructural features, such as carbides. The grain boundaries observed in Alloy C that were spatially located near to carbides contained lower Mn and C levels than grain boundaries that were not located in close proximity (< 40 nm) to carbides. Another factor that may account for the variance in grain boundary compositions within Alloy C is each boundary's physical structure. Similar variations in grain boundary segregation have been reported as a function of misorientation and plane in other steels[41].

Due to the dependence of grain boundary composition on physical structure and spatial location, it is likely that there is also variance in their composition prior to irradiation. As no grain boundaries were characterised via APT in their as-received state, and because the physical structures of the majority of the boundaries in this study are unknown, it is not possible to say with confidence if or how the composition of the grain boundaries has changed during irradiation. However, there is a large degree of enrichment in comparison to the alloys' nominal compositions, and previous grain boundary studies on RPV alloys have shown an enrichment in Ni, Si, Mn, and P after exposure to neutron irradiation[42,43].

However, Mn, Ni, Si, and P were present in higher concentrations at all of the grain boundaries than were present in the alloys, based on their nominal compositions. This is consistent with the observations by Miller and Burke[44].

In Alloy C, the segregation behaviour of elements to the grain boundaries was heterogeneous in nature across the plane of the boundary. Clear cluster formation can be seen on the grain boundary in Figure 13 (b). Grain boundary segregation has sometimes been shown be non-uniform across the plane of the boundary[45–48], although this is the first time that the phenomenon has been reported in neutron-irradiated alloys. It is not known how this heterogeneous distribution of solute atoms across a grain boundary influences macroscale properties. However, the knowledge that grain boundary segregation is not homogeneous across the plane of the grain boundary is of great importance, and must be accounted for when modelling grain boundary segregation under neutron irradiation.

The variation in grain boundary composition for grain boundaries from the same alloy, and the large number of potential grain boundary structures that are present in a material, are two of the challenges associated with using APT data to create models that accurately predict changes in grain boundary chemistry during operation. Other approaches, such as

correlative STEM/transmission Kikuchi diffraction, may be better suited to characterising segregation levels to a large number of interfaces. However, these techniques will not permit the structural nature of the grain boundary to be fully determined. Furthermore, APT is the characterisation technique best suited to investigating and quantifying the distribution of solute atoms across internal interfaces. This, more detailed, description of grain boundary segregation is crucial if a truly holistic understanding of the effect of grain boundary segregation on macroscale properties is to be achieved.

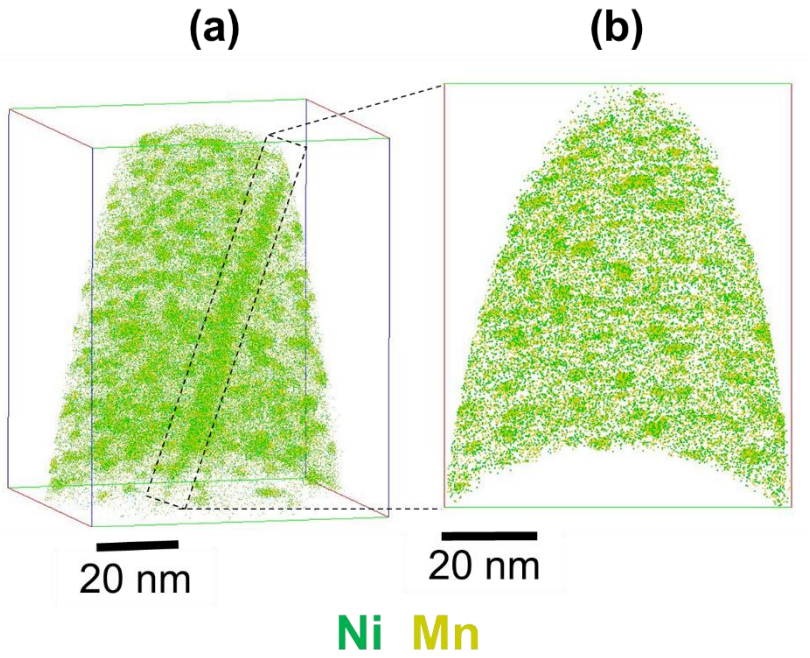

Figure 13: Atom maps for Alloy C showing (a) dataset containing a grain boundary and (b) Planar view of the grain boundary showing the heterogeneous distribution of Mn and Ni atoms across the boundary.

4.6. Effect of Alloy Composition

The systematic variations in composition between the alloys permitted the effect of Ni, Mn and Si levels on the extent of clustering to be made. Alloy C, which contained high levels of Mn, Ni, and Si had the highest number density and volume fraction of clusters after irradiation. Alloy C also displayed the largest hardness increase after irradiation.

Alloy G, which had a lower Ni level than Alloy C, had a much lower number density and volume fraction of clusters. Meanwhile, Alloy K had a lower Mn content than Alloy C and the observed degree of clustering in Alloy K was lower than Alloy C. Whilst one must be careful not to draw too strong conclusions from such small sample sizes, it appears as though increasing Ni and Mn levels are correlated with increased hardness changes, cluster number densities and volume fractions. The effect of Si on cluster formation is less clear.

The composition of the alloys also correlated with the composition of the clusters detected within the alloys. The clusters in Alloy K had a stoichiometry very close to Ni_3Si whilst the clusters in Alloys C and G had higher Mn contents, reflecting the higher Mn content of these alloys. The clusters in RX12 had compositions between FeNi and $FeNi_3$.

5. Conclusions

The formation of clusters in four alloys, with systematic variations in their nominal compositions, was characterised by APT after the alloys were irradiated to high fluence. The main conclusions of this study can be summarised as follows:

- The hardness of the alloys increased after irradiation. The level of hardening was correlated with increased cluster volume fraction in three of the alloys. The degree of precipitate formation in Alloys C, G, and K was consistent with those predicted (based on measured bulk composition) by models within the literature.
- The hardening in RX12 appeared to follow a different trend to the other alloys; this may be a result of the clusters containing a high proportion of Fe.
- The majority of the Fe detected in clusters in RX12 was unlikely to be the result of trajectory aberrations and should be included in compositional, volume fraction, and size calculations.
- The evolution of cluster Mn-Ni-Si content with size was investigated and reported in neutron-irradiated RPV steels for the first time, the composition of clusters was found to vary between the smallest and largest quartile of clusters; likely due to cluster compositions tending more towards thermodynamically stable phases as they grow.
- This study was the first to experimentally investigate the effect of nucleation site on cluster composition. Nucleation site was not found to influence composition for the clusters nucleated within the matrix of Alloys C, G, and K. However, the composition of clusters that nucleated within a carbide were significantly different to those that formed in the matrix of Alloy C.
- Increased Ni and Mn levels were correlated with increased cluster number densities and volume fractions.
- Grain boundary compositions were found to significantly vary from specimen-to-specimen. This demonstrates the importance of determining the physical structure and the spatial location, with respect to other microstructural features, of grain boundaries.
- The distribution of solutes across the grain boundary was not homogeneous in the irradiated alloys, with clustering evident on the boundaries. The application of APT to characterise the uniformity of segregation across internal interfaces is likely to be crucial if holistic models are to be produced.

6. Acknowledgements

This work was supported by the U.S. Department of Energy, Office of Nuclear Energy under DOE Idaho Operations Office Contract DE-AC07- 051D14517 as part of a Nuclear Science User Facilities experiment.

7. Funding Sources

Funding: this work was supported by Rolls-Royce Plc. The atom probe facilities at the University of Oxford are funded by the EPSRC (EP/M022803/1). J. O. Douglas would like to acknowledge the funding provided by EPSRC (EP/P005640/1 and EP/P001645/1).

8. Declaration of interest

None

9. Appendix

The following equations were used to calculate cluster volume fraction (V_f), cluster radius (r), and number density (N_d):

1) Volume Fraction

$$V_f = 100 \times \frac{N_{Ranged}^{Cluster} - N_{Fe}^{Cluster}}{N_{Ranged}^{Dataset}}$$

Where $N_{Ranged}^{Cluster}$ is the number of ranged atoms in all of the clusters, $N_{Fe}^{Cluster}$ is the number of Fe atoms detected in all of the clusters, and $N_{Ranged}^{Dataset}$ is the total number of ranged atoms in the dataset.

2) Cluster Radius

$$r = \left(\frac{3V_{Cluster}}{4\pi}\right)^{1/3}$$

Where $V_{Cluster}$ is the volume of the cluster and is determined as follows:

$$V_{Cluster} = \frac{N_{Ranged}^{Cluster} - N_{Fe}^{Cluster}}{\eta \times \rho_{\alpha-Fe}}$$

Where $N_{Ranged}^{Cluster}$ is the total number of ranged atoms in a cluster, $N_{Fe}^{Cluster}$ is the number of Fe atoms detected in the cluster, η is the detection efficiency of the instrument used, and $\rho_{\alpha-Fe}$ is the number of Fe atoms expected per cubic metre in $\alpha - Fe$.

3) Number Density

$$N_d = \frac{N_{Clusters\ Detected} - (0.5 \times N_{EdgeDetected})}{V_{Dataset}}$$

Where $N_{Clusters\ Detected}$ is the number of clusters detected in the dataset, $N_{EdgeDetected}$ is the number of detected clusters that intersect the edge of the analysed volume, and $V_{Dataset}$ is the volume of the reconstructed dataset. $V_{Dataset}$ was calculated using the equation:

$$V_{Dataset} = \frac{N_{Ranged}}{\eta \times \rho_{\alpha-Fe}}$$

Where N_{Ranged} is the total number of ranged atoms in the dataset, η is the detection efficiency of the instrument used, and $\rho_{\alpha-Fe}$ is the number of Fe atoms expected per cubic metre in $\alpha - Fe$.

Bibliography

1. Odette, G. R. & Nanstad, R. K. Predictive reactor pressure vessel steel irradiation embrittlement models: Issues and opportunities. *J. Mater.* **61**, 17–23 (2009).
2. Miller, M. K. & Burke, M. G. Characterization Of Irradiated A533B Pressure-Vessel Steel Weld. *J. Phys. Colloq.* **48**, 429–434 (1987).
3. Miller, M. K., Russell, K. F., Sokolov, M. A. & Nanstad, R. K. APT characterization of

irradiated high nickel RPV steels. *J. Nucl. Mater.* **361**, 248–261 (2007).

4. Pareige, P., Auger, P., Bas, P. & Blavette, D. Direct observation of copper precipitation in a neutron irradiated FeCu alloy by 3D atomic tomography. *Scr. Metall. Mater.* **33**, 1033–1036 (1995).

5. Pareige, P. & Miller, M. K. Characterization of neutron-induced copper-enriched clusters in pressure vessel steel weld: an APFIM study. *Appl. Surf. Sci.* **94**–**95**, 370–377 (1996).

6. Odette, G. R. On the dominant mechanism of irradiation embrittlement of reactor pressure vessel steels. *Scr. Metall.* **17**, (1983).

7. Odette, G. R., Liu, C. L. & Wirth, B. D. On the composition and structure of nanoprecipitates in irradiated pressure vessel steels. in *Mat. Res. Soc. Sypm. Proc. Vol. 439* 457 (1997).

8. Auger, P., Pareige, P., Akamatsu, M. & Blavette, D. APFIM Investigation of Clustering in Neutron-Irradiated Fe-Cu Alloys and Pressure Vessel Steels. *J. Nucl. Mater.* **225**, 225–230 (1995).

9. Odette, G. R. Radiation induced microstructural evolution in reactor pressure vessel steels. in *Materials Research Society Symposium - Proceedings* **373**, (1995).

10. Miller, M. K., Powers, K. A., Nanstad, R. K. & Efsing, P. Atom probe tomography characterizations of high nickel, low copper surveillance RPV welds irradiated to high fluences. *J. Nucl. Mater.* **437**, (2013).

11. Xiong, W. *et al.* Thermodynamic models of low temperature Mn-Ni-Si precipitation in reactor pressure vessel steels. *Mater. Res. Soc. Commun.* **4**, 101–105 (2014).

12. Wells, P. B. *et al.* Evolution of manganese-nickel-silicon-dominated phases in highly irradiated reactor pressure vessel steels. *Acta Mater.* **80**, (2014).

13. Bergner, F., Ulbricht, A. & Viehrig, H.-W. Acceleration of irradiation hardening of low-copper reactor pressure vessel steel observed by means of SANS and tensile testing. *Philos. Mag. Lett.* **89**, 795–805 (2009).

14. Glade, S. C., Wirth, B. D., Odette, G. R. & Asoka-Kumar, P. Positron annihilation spectroscopy and small angle neutron scattering characterization of nanostructural features in high-nickel model reactor pressure vessel steels. *J. Nucl. Mater.* **351**, 197–208 (2006).

15. Edmondson, P. D., Parish, C. M. & Nanstad, R. K. Using complimentary microscopy methods to examine Ni-Mn-Si-precipitates in highly-irradiated reactor pressure vessel steels. *Acta Mater.* **134**, 31–39 (2017).

16. Nikolaeva, A. V., Nikolaev, Y. A. & Kevorkyan, Y. R. Grain-boundary segregation of phosphorus in low-alloy steel. *At. Energy* **91**, 534–542 (2001).

17. Chen, X.-M., Song, S.-H., Weng, L.-Q., Liu, S.-J. & Wang, K. Relation of ductile-to-brittle transition temperature to phosphorus grain boundary segregation for a Ti-stabilized interstitial free steel. *Mater. Sci. Eng. A* **528**, 8299–8304 (2011).

18. ASTM International. *ASTM E384-17, Standard Test Method for Microindentation Hardness of Materials*. (2017). doi:10.1520/E0384-17

19. Miller, M. K., Russell, K. F. & Thompson, G. B. Strategies for fabricating atom probe specimens with a dual beam FIB. *Ultramicroscopy* **102**, 287–298 (2005).

20. Thompson, K. *et al.* In situ site-specific specimen preparation for atom probe

tomography. *Ultramicroscopy* **107**, 131–139 (2007).

21. Moody, M. P., Stephenson, L. T., Liddicoat, P. V. & Ringer, S. P. Contingency Table Techniques for Three Dimensional Atom Probe Tomography. *Microsc. Res. Tech.* **70**, 258 (2007).

22. Hyde, J. M. & English, C. A. An Analysis of the Structure of Irradiation induced Cu-enriched Clusters in Low and High Nickel Welds. in *Cited by 19 Get access Volume 650 (Symposium R – Microstructural Processes in Irradiated Materials)* R6.6 (2000). doi:https://doi.org/10.1557/PROC-650-R6.6

23. Hyde, J. M., Marquis, E. A., Wilford, K. B. & Williams, T. J. A sensitivity analysis of the maximum separation method for the characterisation of solute clusters. *Ultramicroscopy* **111**, 440–447 (2011).

24. Cerezo, A. & Davin, L. Aspects of the observation of clusters in the 3-dimensional atom probe. *Surf. Interface Anal.* **39**, 184–188 (2007).

25. Vurpillot, F., Bostel, A. & Blavette, D. Trajectory overlaps and local magnification in three-dimensional atom probe. *Appl. Phys. Lett.* **76**, 3127–3129 (2000).

26. Shu, S., Wirth, B. D., Wells, P. B., Morgan, D. D. & Odette, G. R. Multi-technique characterization of the precipitates in thermally aged and neutron irradiated Fe-Cu and Fe-Cu-Mn model alloys: Atom probe tomography reconstruction implications. *Acta Mater.* **146**, 237–252 (2017).

27. Jenkins, B. M. *et al.* Using alpha hulls to automatically and reproducibly detect edge clusters in atom probe tomography datasets. *Mater. Charact.* **160**, 110078 (2020).

28. Jenkins, B. M. Improving The Safety and Reliability of RPV Steels. (University of Oxford, 2019).

29. Blavette, D., Vurpillot, F., Pareige, P. & Menand, A. A model accounting for spatial overlaps in 3D atom-probe microscopy. *Ultramicroscopy* **89**, 145–153 (2001).

30. Felfer, P. J. *et al.* A New Approach to the Determination of Concentration Profiles in Atom Probe Tomography. *Microsc. Microanal.* **18**, 359–364 (2012).

31. London, A. J. AtomProbeLab. https://sourceforge.net/projects/atomprobelab/ (2019).

32. London, A. J. Quantifying Uncertainty from Mass-Peak Overlaps in Atom Probe Microscopy. *Microsc. Microanal.* 1–11 (2019). doi:10.1017/S1431927618016276

33. Almirall, N. *et al.* Precipitation and Hardening in Irradiated Low Alloy Steels with a Wide Range of Ni and Mn Compositions. *Acta Mater.* **Manuscript**, 119–128 (2018).

34. Russell, K. C. & Brown, L. M. A dispersion strengthening model based on differing elastic moduli applied to the iron-copper system. *Acta Metall.* **20**, 969–974 (1972).

35. Worrall, G. M. & Smith, G. D. W. The quantitative analysis of copper in iron based alloys. *J. Phys. Colloq.* **47**, 245–250 (1986).

36. Morley, A., Sha, G., Hirosawa, S., Cerezo, A. & Smith, G. D. W. Determining the composition of small features in atom probe: bcc Cu-rich precipitates in an Fe-rich matrix. *Ultramicroscopy* **109**, 535–540 (2009).

37. Gault, B., Moody, M. P., Cairney, J. M. & Ringer, S. P. *Atom Probe Microscopy*. *Springer Series in Materials Science* (Springer-Verlag New York, 2012). doi:10.1007/978-1-4614-3436-8

38. Swartzendruber, L. J., Itkin, V. P. & Alcock, C. B. The Fe-Ni (iron-nickel) system. *J.*

Phase Equilibria **12**, 288–312 (1991).

39. Belkacemi, L. T., Meslin, E., Décamps, B., Radiguet, B. & Henry, J. Radiation-induced bcc-fcc phase transformation in a Fe-3%Ni alloy. *Acta Mater.* **161**, 61–72 (2018).

40. Shu, S., Wells, P. B., Almirall, N., Odette, G. R. & Morgan, D. D. Thermodynamics and kinetics of core-shell versus appendage co-precipitation morphologies: an example in the Fe-Cu-Mn-Ni-Si system. *Acta Mater.* **157**, 298–306 (2018).

41. Herbig, M. *et al.* Atomic-scale quantification of grain boundary segregation in nanocrystalline material. *Phys. Rev. Lett.* **112**, 1–5 (2013).

42. Fedotova, S. V., Kuleshova, E. A., Maltsev, D. A. & Saltykov, M. A. Complex study of grain boundary segregation in long-term irradiated reactor pressure vessel steels. *J. Nucl. Mater.* **528**, 151865 (2020).

43. Kuleshova, E. A. *et al.* Study of the flux effect nature for vver-1000 RPV welds with high nickel content. *J. Nucl. Mater.* **483**, 1–12 (2017).

44. Miller, M. K. & Burke, M. G. An APFIM Survey Of Grain Boundary Segregation And Precipitation In Irradiated Pressure Vessel Steels. *ASTM STP* **1175**, 492 (1993).

45. Zhao, H. *et al.* Segregation assisted grain boundary precipitation in a model Al-Zn-Mg-Cu alloy. *Acta Mater.* **156**, 318–329 (2018).

46. Kwiatkowski Da Silva, A. *et al.* Phase nucleation through confined spinodal fluctuations at crystal defects evidenced in Fe-Mn alloys. *Nat. Commun.* **9**, 1–11 (2018).

47. Li, L. *et al.* Segregation-driven grain boundary spinodal decomposition as a pathway for phase nucleation in a high-entropy alloy. *Acta Mater.* **178**, 1–9 (2019).

48. Peng, Z. *et al.* An Automated Computational Approach for Complete In-Plane Compositional Interface Analysis by Atom Probe Tomography. *Microsc. Microanal.* 1–12 (2019). doi:10.1017/S1431927618016112